Simulations of drift resistive ballooning L-mode turbulence in the edge plasma of the DIII-D tokamak

B. I. Cohen, M. V. Umansky, W. M. Nevins, M. A. Makowski, J. A. Boedo et al.

Additional information on Phys. Plasmas

Simulations of drift resistive ballooning L-mode turbulence in the edge plasma of the DIII-D tokamak[a]

B. I. Cohen,[1,b] M. V. Umansky,[1] W. M. Nevins,[1] M. A. Makowski,[1] J. A. Boedo,[2]
D. L. Rudakov,[2] G. R. McKee,[3] Z. Yan,[3] and R. J. Groebner[4]

[1]*Lawrence Livermore National Laboratory, Livermore, California 94550, USA*
[2]*University of California, San Diego, San Diego, California 92093, USA*
[3]*University of Wisconsin-Madison, Madison, Wisconsin 53706, USA*
[4]*General Atomics, P.O. Box 85608, San Diego, California 92186, USA*

Results from simulations of electromagnetic drift-resistive ballooning turbulence for tokamak edge turbulence in realistic single-null geometry are reported. The calculations are undertaken with the BOUT three-dimensional fluid code that solves Braginskii-based fluid equations [X. Q. Xu and R. H. Cohen, Contrib. Plasma Phys. **36**, 158 (1998)]. The simulation setup models L-mode edge plasma parameters in the actual magnetic geometry of the DIII-D tokamak [J. L. Luxon *et al.*, Fusion Sci. Technol. **48**, 807 (2002)]. The computations track the development of drift-resistive ballooning turbulence in the edge region to saturation. Fluctuation amplitudes, fluctuation spectra, and particle and thermal fluxes are compared to experimental data near the outer midplane from Langmuir probe and beam-emission-spectroscopy for a few well-characterized L-mode discharges in DIII-D. The simulations are comprised of a suite of runs in which the physics model is varied to include more fluid fields and physics terms. The simulations yield results for fluctuation amplitudes, correlation lengths, particle and energy fluxes, and diffusivities that agree with measurements within an order of magnitude and within factors of 2 or better for some of the data. The agreement of the simulations with the experimental measurements varies with respect to including more physics in the model equations within the suite of models investigated. The simulations show stabilizing effects of sheared $E \times B$ poloidal rotation (imposed zonal flow) and of lower edge electron temperature and density. © 2013 AIP Publishing LLC. [http://dx.doi.org/10.1063/1.4804638]

I. INTRODUCTION

The edge region of tokamak plasmas continues to be an active research area because of its importance in influencing particle and energy confinement in the plasma as a whole,[1] the importance of the plasma interaction with the divertor plates and the wall of the vacuum vessel,[2] and the richness of the collective phenomena in the edge. The edge plasma is subject to plasma turbulence that degrades energy and particle confinement and can include transient events like the Edge Localized Mode (ELM) as well as the formation of filamentary structures. Understanding the turbulence in the tokamak edge plasma is challenging to theory and modeling. Direct numerical simulation has become a useful tool for exploring physics of tokamak edge plasma turbulence because the physics and tokamak geometry are too complex for analytical theory.

The direct simulation in realistic geometry of turbulence in L-mode discharges in the DIII-D tokamak[3] edge plasma is useful for understanding turbulence in tokamak edge plasmas. These L-mode discharges exhibit stationary steady-states and are less complex for modeling than are H-mode discharges. In this work comparisons of the simulation results to DIII-D L-mode data from experimental diagnostics are reported. Experimental observations and transport analyses have established that the edge region of L-mode tokamak plasmas exhibits anomalous transport of particles and energy.[4] There are strong gradients in the edge region that provide drive mechanisms for collective modes of instability that can lead to the observed anomalous transport. Antecedents for the work presented here are the earlier studies by Carreras and co-workers,[5,6] and by Guzdar, Drake and co-workers[7–11] wherein resistive interchange, resistive ballooning, and drift-resistive ballooning modes were considered. The theory of resistive interchange modes traces back to the earlier classic papers of Furth *et al.*[12] and Coppi.[13] The references cited here are intended as representative examples of a larger body of work.

The simulation results and comparison to L-mode discharge data from DIII-D reported here based on the drift-resistive ballooning physics model are inspired by the earlier work of Carreras *et al.*, and Guzdar *et al.*, using plasma fluid equations solved numerically[14–17] in a realistic, single-null geometry for DIII-D for conditions specific to a series of well-characterized L-mode discharges. Detailed comparisons are shown for the simulation results and experimental data provided by a scanning Langmuir probe[18–20] and beam-emission spectroscopy (BES)[21–23] where available for DIII-D shots #119 919 and 119 934. These shots are both L-mode discharges; shot #119 934 has somewhat lower edge plasma density and electron temperature than in #119 919.

The principal results here are that simulations based on the drift-resistive ballooning model yield fluctuation

amplitudes, particle and heat fluxes, inferred transport coefficients, correlation lengths, and spectra that agree with experiment within an order of magnitude and within factors of 2 or better for some of the data. The agreement of the simulations with the experimental measurements varies with respect to including more physics in the model equations within the suite of models investigated.

The paper is organized as follows. The Introduction is followed in Sec. II by a description of the model equations and the simulation methodology. Section III presents a discussion of the simulation results and the diagnostics in the simulations, and comparison to the experimental data. The paper concludes in Sec. IV with a summary discussion. There is an appendix providing the specification of input profiles for the simulations.

II. MODEL EQUATIONS FOR EDGE TURBULENCE

The model equations for fluid turbulence in tokamak edge region are predicated on the validity of the assumption that the edge plasma is sufficiently collisional. The Braginskii[24] two-fluid equations in drift ordering for a strongly magnetized, collisional plasma[25–28] provide the foundation for the model equations used for the simulations. The model equations used are a simplified, reduced set of equations that embody the physics of drift-resistive ballooning in an electromagnetic model that can include temperature fluctuations for both electron and ion species. The reduction of the Braginskii equations in the drift ordering to the simpler set of equations used here is somewhat arbitrary but illustrates various physics terms and shares the philosophy of earlier published work exploring model equations for edge turbulence.[5–11] For example, the evolution equations for the temperature fluctuations are much simplified and include only $\mathbf{E} \times \mathbf{B}$ convection and parallel thermal conduction.

The dynamical equations in our model describe the time-evolution of non-axisymmetric fluctuations of plasma density $\tilde{N}_i$, the potential vorticity $\tilde{\varpi}$, electron parallel velocity $\tilde{v}_{\|e}$, ion parallel velocity $\tilde{v}_{\|i}$, electron temperature $\tilde{T}_e$, and ion temperature $\tilde{T}_i$. Here, the notation is $f = f_0 + \tilde{f}$, where the subscript 0 represents the underlying axisymmetric equilibrium quantities that are not evolved in time; the tilde symbol represents the non-axisymmetric perturbations that are evolved; and the sum represents the total

$$\frac{d\tilde{N}_i}{dt} + v_{\|i}\vec{b}_0 \cdot \nabla N_i + N_i \nabla_\| v_{\|i}$$
$$= \left(\frac{2c}{eB}\right)\vec{b}_0 \times \vec{\kappa} \cdot (\nabla \tilde{P}_e - N_i e \nabla \tilde{\phi}) + \nabla_\| \left(\frac{\tilde{j}_\|}{e}\right), \quad (1)$$

$$\frac{d\tilde{\varpi}}{dt} = 2\omega_{ci}\vec{b}_0 \times \vec{\kappa} \cdot \nabla \tilde{P}_{ei} + N_i Z_i e \frac{4\pi V_A^2}{c^2} \nabla_\| \tilde{j}_\|, \quad (2)$$

$$\frac{d\tilde{v}_{\|e}}{dt} = -\frac{e}{m_e}\tilde{E}_\| - \frac{1}{N_i m_e} T_e \partial_\| \tilde{N}_i + 0.51\nu_{ei}(\tilde{v}_{\|i} - \tilde{v}_{\|e}), \quad (3)$$

$$\frac{d\tilde{v}_{\|i}}{dt} = -\frac{1}{N_i M_i}\partial_\| \tilde{P}_{ei}, \quad (4)$$

$$\frac{d\tilde{T}_e}{dt} = \frac{2}{3N_i}\nabla_\|(\kappa_\|^e \partial_\| \tilde{T}_e), \quad (5)$$

$$\frac{d\tilde{T}_i}{dt} = \frac{2}{3N_i}\nabla_\|(\kappa_\|^i \partial_\| \tilde{T}_i), \quad (6)$$

where the various auxiliary quantities are defined as follows:

$$\frac{d}{dt} = \frac{\partial}{\partial t} + \vec{V}_E \cdot \nabla, \quad \vec{V}_E = c\vec{b}_0 \times \nabla_\perp \phi/B,$$

$$E_\| = -\partial_\| \phi - (1/c)\frac{\partial A_\|}{\partial t},$$

$$\varpi = N_i q \nabla_\perp^2 \phi + N_i q \nabla_\perp \phi \cdot \nabla_\perp \ln N_i + \nabla_\perp^2 P_i \approx N_i q \nabla_\perp^2 \phi,$$

$$\nabla_\perp^2 A_\| = -(4\pi/c)j_\|, \quad \vec{\tilde{B}} = \nabla A_\| \times \vec{b}_0, \quad \nabla_\| F = B\partial_\|(F/B),$$

$$\partial_\| = \partial_\|^0 + \vec{\tilde{b}} \cdot \nabla, \quad \vec{\tilde{b}} = \vec{\tilde{B}}/B, \quad \partial_\|^0 = \vec{b}_0 \cdot \nabla,$$

$$\vec{\kappa} = \vec{b}_0 \cdot \nabla \vec{b}_0, \quad j_\| = -eN_i v_{\|e}, \quad P_{e,i} = N_i T_{e,i},$$

$$\tilde{P}_{e,i} = \tilde{N}_i T_{e,i} + N_i \tilde{T}_{e,i}.$$

Here, the standard notation is used: E is the electric field, $A_\|$ is the parallel component of the vector potential, B is the magnetic field, e is the electron charge, and $\kappa_\|^{e,i}$ is the electron/ion parallel thermal conduction.

Equations ((1)–(6)) do not assume that the fluctuations are small. However, the relation between the electric potential and vorticity $\varpi = N_i q \nabla_\perp^2 \phi$ is simplified from the full form, as given in Ref. 14, using the Boussinesq approximation. This takes advantage of the separation of spatial scales of turbulence and background profiles, $k_\perp L_{n,T} \gg 1$; and relies on the smallness of the density fluctuations, $\tilde{N}_i/N_{i0} \ll 1$. These assumptions are reasonably well satisfied in the simulations reported here, $k_\perp L_{n,T} \sim 10$ and $\tilde{N}_i/N_{i0} \lesssim 30\%$. However, the Laplacian of the ion pressure fluctuation is dropped in relating the vorticity to electrostatic potential to simplify the model. Various fluxes and transport coefficients used for comparison with experimental data are the radial particle flux $\Gamma_\perp$, electron conductive heat flux $q_{\perp,e}^{cond}$, electron convective heat flux $q_{\perp,e}^{conv}$, and the corresponding diffusivities defined as

$$\Gamma_\perp = \langle \tilde{N}_i \tilde{v}_r \rangle_{\zeta,t}, \quad q_{\perp,e}^{cond} = \frac{3}{2}N_{i0}\langle \tilde{v}_r \tilde{T}_e \rangle_{\zeta,t}, \quad q_{\perp,e}^{conv} = \frac{3}{2}T_{e0}\Gamma_\perp,$$

$$q_{\perp,e}^{total} = q_{\perp,e}^{conv} + q_{\perp,e}^{cond}, \quad D_\perp = -\frac{\Gamma_\perp}{\nabla N_{i0}}, \quad \chi_{\perp,e}^{cond} = -\frac{q_{\perp,e}^{cond}}{N_{i0}\nabla T_{e0}}$$

$$\chi_{\perp,e}^{total} = -\frac{q_{\perp,e}^{total}}{N_{i0}\nabla T_{e0}},$$

where the subscripts ζ, t stand for averaging in the toroidal angle and time.

The system of equations Eqs. ((1)–(7)) forms the largest set used in the simulations reported here. Several smaller subsets of this system were used for analyzing the sensitivity of the results to particular terms.

- Case 1: $\tilde{T}_i = 0$, $\tilde{T}_e = 0$, $\tilde{b} = 0$, $\phi_0 = 0$.
  — Case 1a: $\phi_0 = \phi_0(x)$
- Case 2: $\tilde{T}_i = 0$, $\tilde{T}_e \neq 0$ however $\kappa_\|^e = 0$; $\tilde{b} = 0$, $\phi_0 = 0$

- Case 3: $\tilde{T}_i = 0$, $\tilde{T}_e \neq 0$, $\tilde{b} = 0$, $\phi_0 = 0$
- Case 4: $\tilde{T}_i = 0$, $\tilde{T}_e \neq 0$, $\tilde{b} \neq 0$, $\phi_0 = 0$
- Case 5: $\tilde{T}_i \neq 0$, $\tilde{T}_e \neq 0$, $\tilde{b} \neq 0$, $\phi_0 = 0$
- Case 6: $\tilde{T}_i \neq 0$, $\tilde{T}_e \neq 0$, $\tilde{b} \neq 0$, $\phi_0 = 0$

  — Case 6a: $\phi_0 = \phi_0(x)$
  — Case 6b: $\phi_0 = 5 \times \phi_0(x)$

Case 1 is the simplest in the list: it includes only Eqs. ((1)–(4)) and does not include $\tilde{b} \cdot \nabla$ terms. However, these equations support the drift-resistive ballooning mode physics,[5–11,15–17,27] which is enough to capture the main features of instability growth and resulting turbulence. Case 6 is the most complete system: it includes all terms in Eqs. ((1)–(6)).

The dynamic equations Eqs. ((1)–(6)) determine the time-evolution for non-axisymmetric components of all fluid variables, while the axisymmetric toroidal field components N_{i0}, $T_{e,i0}$, and ϕ_0 are fixed by the defined initial profiles matched to experimental probe data and are not evolved. The choice of N_{i0}, $T_{e,i0}$, and ϕ_0 profiles is discussed further in the text and in the Appendix. Note that a completely self-consistent determination of the axisymmetric profiles in the simulation would require proper inclusion of sources and sinks for plasma and energy, interaction of the plasma with neutrals and plasma facing components which would make it a formidable multiscale problem in time and space. On the other hand, based on the strong separation of time-scales for turbulence and axisymmetric transport in this problem, it is reasonable to take the axisymmetric components as frozen in time, which is the choice made in this study.

The numerical solution of equations in BOUT is described in the published literature, Refs. 15–17 and 27. The present study uses BOUT as described in Ref. 28, but in the future this work will transition to the more modern edge modeling framework BOUT++.[17] The equations are solved as an initial-value problem on a three-dimensional spatial mesh, and the mesh is based on the reconstruction computed with the equilibrium reconstruction code EFIT.[53] The spatial mesh is generated using the UEDGE code.[29] For tokamak simulations, BOUT uses quasi-ballooning coordinates with twist-shift periodic boundary conditions wrapping around the torus toroidally and poloidally, and with radial boundary conditions on the fields or their radial derivatives.[28] An odd-even numerical mode is controlled in the simulations reported here by inclusion of a numerical hyper-viscosity term $-\alpha \nabla_\parallel^4$ on the right sides of Eqs. ((1)–(6)) with α chosen so that the Nyquist mode has amplification factor less than unity, while the physical modes of interest at longer parallel

wavelength are negligibly influenced by the numerical viscosity. Various benchmarks to verify the BOUT code are documented in published literature.[16,28,30,31]

The simulation domain is a periodic toroidal wedge. In the simulations reported here, for most cases the toroidal domain size is $2\pi/N_w$ where $N_w = 16$, and the toroidal grid size uses $N_z = 64$ grid points. Thus, the toroidal mode numbers represented on the grid range from $N_w = 16$ to $N_w \times N_z/2 = 512$ (although the upper third of the spectrum is poorly represented due to the usual finite-difference effects). The simulations results reported here are not sensitive to doubling the toroidal domain size (while simultaneously doubling N_z). The radial domain size used is $0.9 < \psi_{norm} < 1.15$. At the outer midplane this translates to $0.98 \leq R/R_{sep} \leq 1.03$, where R_{sep} is the major radius at the location of the magnetic separatrix. For most of the simulations, a relatively coarse radial grid was used, with $N_r = 40$ grid points, to speed up the throughput. In simulations with double radial resolution, the saturated amplitudes for $\tilde{N}_i$, $\tilde{T}_e$, $\tilde{T}_i$, $\tilde{\phi}$ are within 10%-20% of those with the coarser radial grid, and thus, the grid resolution is considered sufficient for this scoping study aiming to establish relevance of the model to the experiment. Furthermore, as discussed subsequently in the text, in the simulations results no significant spectral power is observed in the saturated density fluctuation power spectrum beyond the radial wavenumber $k_r \sim 5$ [rad/cm] while the radial Nyquist wavenumber is larger than that by a factor of 2.5, which confirms that the radial resolution is sufficient for capturing the gross features of the studied turbulence.

III. SIMULATIONS AND COMPARISON TO EXPERIMENTAL DATA

A. Edge plasma turbulence in shot #119 919

The first shot studied is #119 919, which is a well-characterized DIII-D L-mode discharge that exhibits steady-state turbulence. For the simulations, the plasma profiles and EFIT equilibrium-reconstruction data are taken from the DIII-D database and the computational mesh is constructed using the grid-generator built in the UEDGE code. Then a suite of BOUT runs is carried out for the cases defined in Sec. II.

In the simulations, plasma instabilities start from a small initial seed, go through a linear growth phase, and then progress to a saturated state (Fig. 1). Figures 1–5 show results comparing cases 4 (includes T_e fluctuations but not T_i fluctuations) and 5 (includes both T_e and T_i fluctuations). Case 5 exhibits a faster linear growth rate (Fig. 1) and saturates at
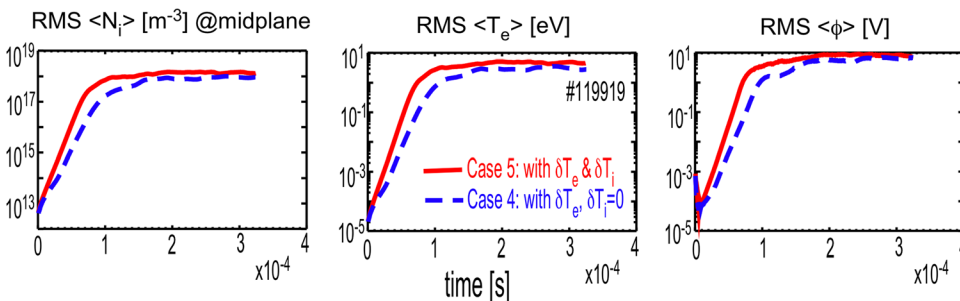

FIG. 1. RMS average with respect to the toroidal angle of the ion density, electron temperature, and electrostatic potential fluctuations at the separatrix in the outer midplane vs. time for cases 4 and 5 simulations of shot #119 919.

(a) RMS <Ni> [m-3]
(b) RMS Ion Density Fluct [m-3]
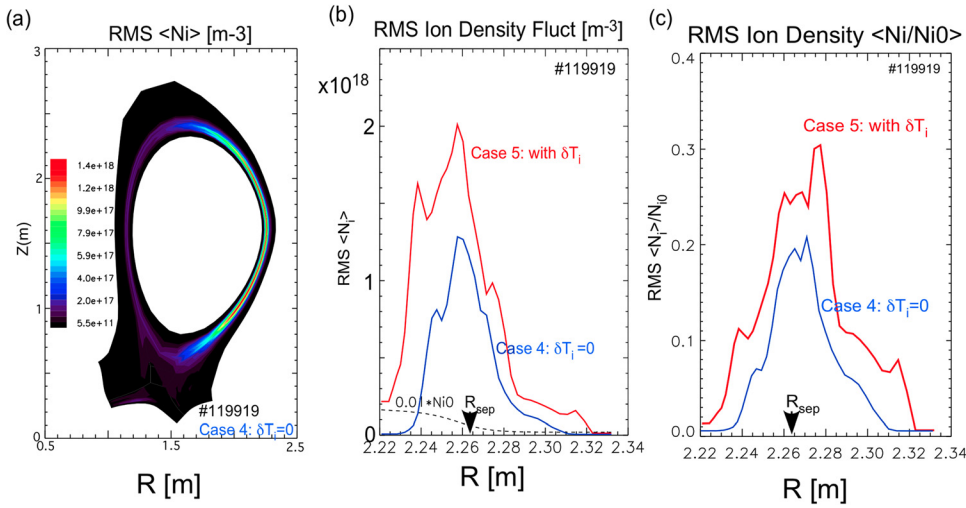(c) RMS Ion Density <Ni/Ni0>

FIG. 2. Shot #119 919 (a) RMS ion density fluctuation vs. R and Z at saturation for case 4 simulation of #119 919; (b) RMS ion density fluctuations vs. R in the midplane for cases 4 and 5; and (c) ratio of the RMS ion density fluctuation to the background ion density vs. R in the midplane for cases 4 and 5.

modestly higher amplitudes than does case 4 without T_i fluctuations. With finite electron and ion temperature fluctuations there is increased interchange drive through the pressure weighted curvature in the vorticity equations, Eq. (2), if the equilibrium temperature and density radial gradients share the same sign (<0) on the outside of the torus where there is bad curvature. With the unperturbed equilibrium gradients fixed and self-consistent zonal flow generation precluded, the saturated steady-state turbulence results from the nonlinear terms in Eqs. ((1)–(6)) mediating a balance between the linearly unstable modes and the damped modes with finite toroidal mode numbers. Such a mechanism for saturation of fluid turbulence is well established in the fluid dynamics and plasma physics literature.[32]

At saturation (Figs. 2–5), the turbulence is dominant on the outboard side of the tokamak, peaks near the outer midplane and near the separatrix, and extends a few centimeters on either side of the separatrix. Note that in all R-Z two-dimensional contour plots of the fluctuations, Z denotes a vertical Cartesian coordinate distinguished from the toroidal-like z BOUT coordinate. All plotted densities, temperatures and electric potential quantities that are denoted as RMS (root-mean-square average with respect to toroidal angle) or fluctuating are the perturbed time-dependent quantities $\tilde{f}$ and do not include the time-independent equilibrium values f_0.

Another visualization of the ballooning nature of the turbulence is shown in Fig. 6 which plots the RMS density fluctuation and the relative density fluctuation as a function of radius in the outer midplane and as a function of the poloidal angle on the separatrix for case 1 (all of the cases share this structure).

The relative electron density fluctuations reach 20%-30% near the separatrix (Fig. 2), and the peak electron temperature fluctuations are of order 50% (Fig. 3). The electron turbulent particle and thermal fluxes are likewise localized (Figs. 4 and 5) and are dominant on the outboard side and very small on the inboard side. The strong in-out asymmetry in the fluctuations is apparently caused by the curvature drive on the outer side of the plasma and is consistent with expectations and observed in experiments, for example, on the Alcator C-Mod tokamak.[33] Furthermore, there is an apparent up-down asymmetry, which is probably associated with the presence of the X point in the plasma at the bottom of the cross section and the influence of the X point on the magnetic shear.

Tables I and II summarize the key observables at saturation in the simulations corresponding to the various cases defined in Sec. II. Various fluxes and transport coefficients in Table I are the radial particle flux $\Gamma_\perp$, electron conductive heat flux $q_{\perp,e}^{cond}$, total electron heat flux $q_{\perp,e}^{total}$, and the

(a) RMS <Te> [eV]
(b) RMS Electron Temperature Fluct [eV]
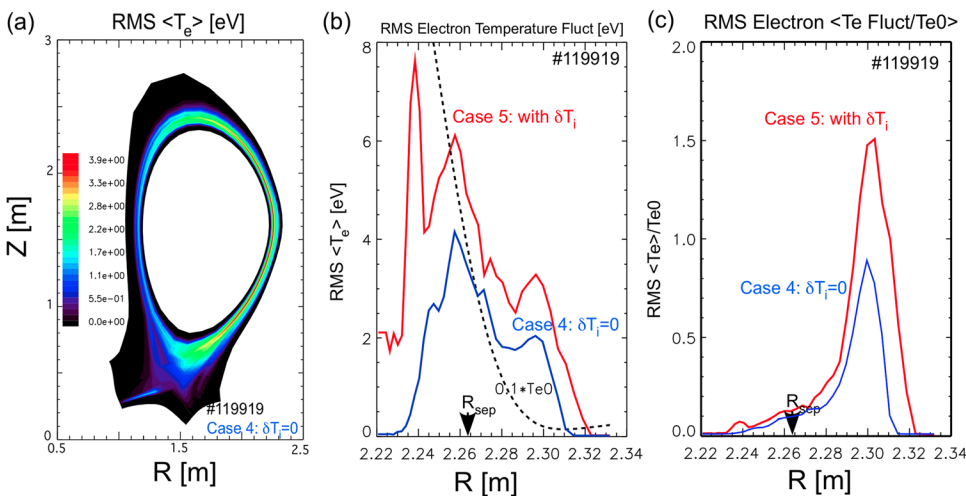(c) RMS Electron <Te Fluct/Te0>

FIG. 3. Shot #119 919 (a) RMS ion density fluctuation vs. R and Z at saturation for case 4 simulation of #119 919; (b) RMS ion density fluctuations vs. R in the midplane for cases 4 and 5; and (c) ratio of the RMS ion density fluctuation to the background ion density vs. R in the midplane for cases 4 and 5.
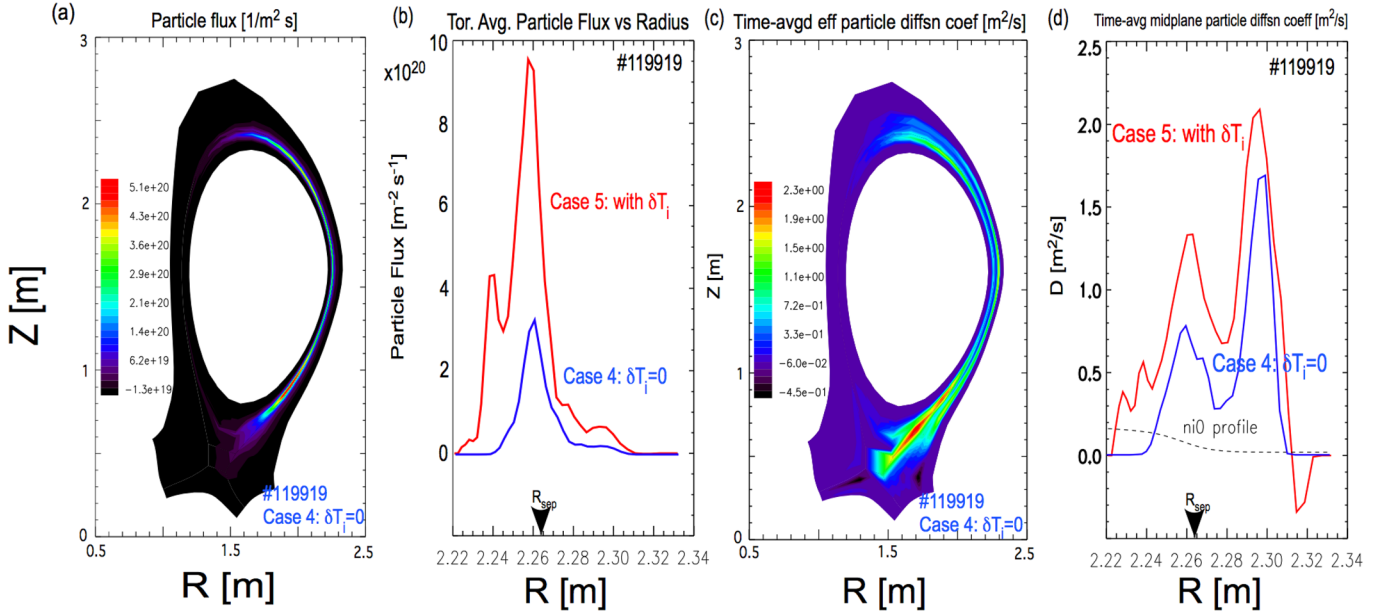
FIG. 4. Shot #119 919 (a) RMS electron temperature fluctuation vs. R and Z at saturation for case 4 simulation; (b) RMS electron temperature fluctuation vs. R in the midplane for cases 4 and 5; and (c) ratio of the RMS electron temperature fluctuation to the background electron temperature vs. R in the midplane for cases 4 and 5.

corresponding diffusivities defined in Sec. II. Note that case 1a did not reach saturated steady-state turbulence at the end of simulation (1.8 ms).

The simulation results shown throughout corresponding to snapshots of fluctuation amplitudes as functions of radius at saturation or the end of the simulation are RMS-averages with respect to the toroidal angle. However, the fluctuation amplitudes still have a temporal variability of ±20%-50%, which should be kept in mind when comparing the simulation data to experiment. At fixed position, the experimental data for the probe have error bars of a few percent; however, the uncertainty of the probe position translates into much larger error bars when comparing simulation and probe data. Measurements with scanning Langmuir probes have been benchmarked against other diagnostic measurements and are documented in the literature.[19,34–36]
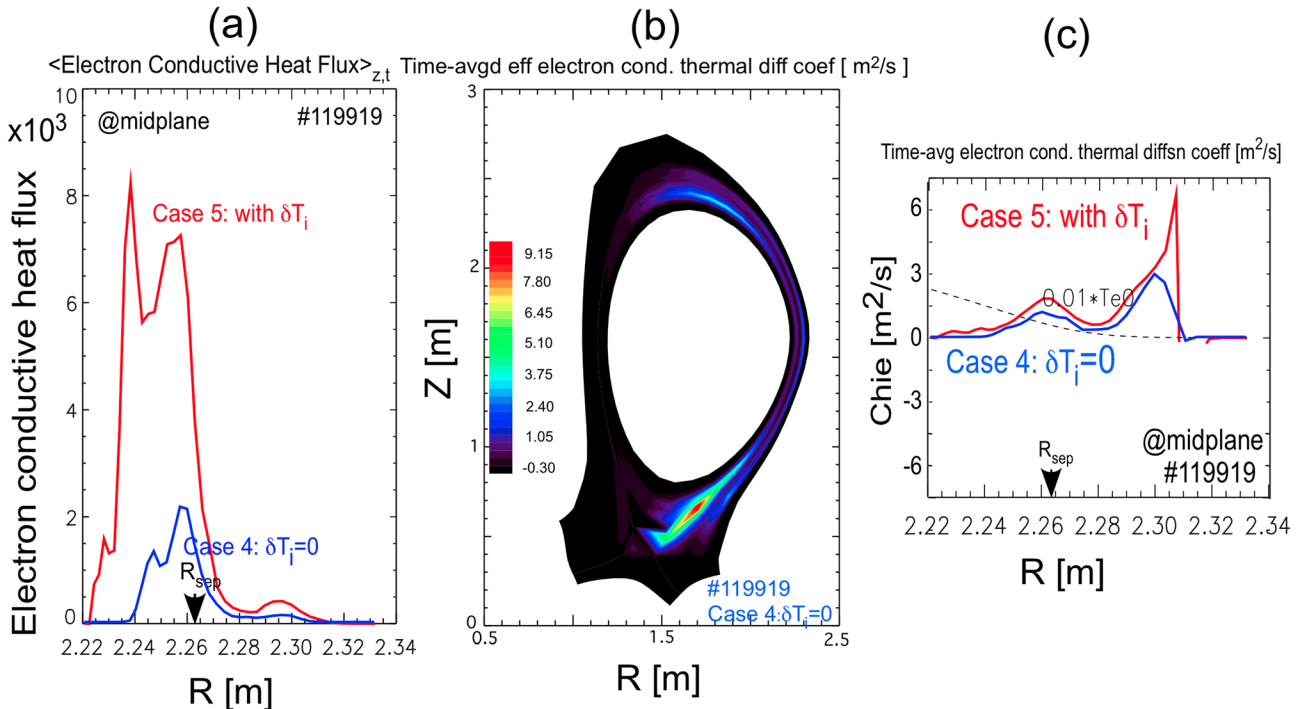

FIG. 5. Shot #119 919 (a) RMS particle flux vs. R and Z at saturation for case 4 simulation; (b) RMS particle flux vs. R in the midplane for cases 4 and 5; (c) RMS particle diffusion coefficient vs. R and Z for cases 4 and 5; and (d) RMS particle diffusion coefficient vs. R in the midplane for cases 4 and 5.
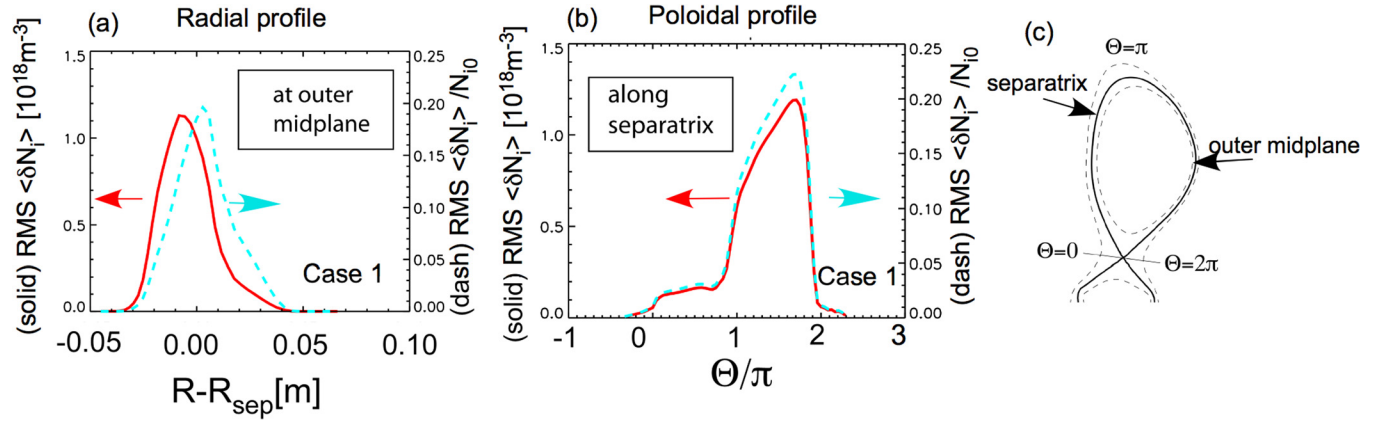
FIG. 6. Shot #119 919 RMS density fluctuation and relative density fluctuation (a) vs. R in the outer midplane at saturation for case 1 simulation and; (b) vs. poloidal angle Θ along the separatrix; (c) schematic showing the poloidal angle coordinate, the separatrix and the outer midplane.

B. Comparison of simulation results to experimental data for shot #119 919

Shot #119 919 in DIII-D is a well-characterized L-mode shot that exhibited steady-state turbulence. Simulation results are compared to data from a scanning Langmuir probe[18] and from BES[21] in Tables I and II, respectively, and in Figs. 7 and 8, respectively. There is no BES data available for #119 919, and the BES data are taken from a similar shot #119 921. Note that comparison of the probe data shown in Fig. 7 with the BES data shown in Fig. 8 indicates agreement in the peak amplitude of the relative density perturbation normalized to the background density $|\tilde{N}_i/N_{i0}| \sim 10\%$ peaking near the separatrix and localization widths 2-4 cm (given the resolution limits of the diagnostics). The relative agreement of the simulations for cases 4, 5, and 6 with respect to the experimental measurements is within an order of magnitude and within a factor of 2 or better for some cases.

In comparing the simulations to the BES data, it is important to take into account the restrictions on spatial resolution set by the BES imaging grid, which has 1 cm separation radially and toroidally in its 4×4 approximately square grid. This restriction on spatial resolution necessitates processing the simulation data through a low-pass filter that mimics the 1 cm limit in resolution. This is accomplished by making use of the GKV software.[37,38] Spatial filtering (1D or 2D) is required in the simulation diagnostics to model the

$\Delta x = 1$ cm limit on spatial resolution in the BES. Filtering is applied to both the radial and binormal coordinates through the convolution of the data with a window function

$$f_{smooth}(x) = \int dx' w(x - x') f(x'), \text{ where}$$

$$w(x) = \begin{cases} \dfrac{1}{2\Delta x}\left[1 + \cos\left(\dfrac{\pi x}{\Delta x}\right)\right] & \left|\dfrac{x}{\Delta x}\right| < 1 \\ 0 & \left|\dfrac{x}{\Delta x}\right| > 1. \end{cases} \quad (7)$$

The correlation functions computed in GKV and shown later are defined by the standard normalized integrals.

Simulation results for case 5 with T_e and T_i fluctuations agree with the probe data for the peak values and relative localization of the density and electron temperature fluctuations and the radial particle flux for $2.25 \text{ m} \leq R \leq 2.31\text{m}$ in Fig. 7 to better than factors of 2, while the peak value of the electron conductive heat flux in the simulation is significantly larger than the probe data. However, the convective component of the electron heat flux measured by the probe $\sim 2.4 \times 10^4 \text{ J m}^{-2} \text{ s}^{-1}$ agrees with the simulation to better than a factor of 2; and the convective heat flux is much larger than the conductive heat flux, so that the agreement between the simulation and the probe data on the total electron heat flux is also better than a factor of 2. The particle and energy

TABLE I. Comparison of BOUT simulations with probe data for DIII-D shot #119 919. The last two columns show data from the scanning Langmuir probe for shot #119 919 are shown and typical, flux-surface-averaged values for shot #119 919 inferred from UEDGE reconstructions.

Simulation case	$\langle \delta N_i \rangle_{rms}$ (10^{18}m^{-3})	$\langle \delta T_e \rangle_{rms}$ (eV)	$\Gamma_\perp$ (10^{20}/m^{2}s)	$D_\perp$ (m^2/s)	$q_\perp^{cond}$ (10^{20}J/m^{2}s)	$\chi_{\perp,e}^{cond}$ (m^2/s)	$q_\perp^{total}$ (10^3J/m^{2}s)	$\chi_{\perp,e}^{total}$ (m^2/s)
#1	0.95	N/A	1.8	0.4	N/A	N/A	…	…
#1a	0.37	N/A	0.07	0.02	N/A	N/A	…	…
#2	1.0	43	4.3	0.77	54	7.2	…	…
#3	0.58	5.8	1.0	0.17	0.72	0.2	…	…
#4	1.3	4.0	3.3	1.7	3.3	2.7	…	…
#5	2.0	7.5	9.5	2.0	10	2.2	22	4
#6a	0.7	5.5	0.8	0.27	2.5	0.32	4.6	0.39
#6b	0.3	3.5	0.18	0.035	0.75	0.036	…	…
Probe	2.0	10	11	…	1.2	…	12	…
UEDGE	…	…	…	0.2-1	…	1-2	…	1-3

TABLE II. Comparison of BOUT simulations with BES data for DIII-D shot #119 919. Shown are the maximum amplitude of relative density fluctuations, their correlation lengths in R and z, the frequency at the peak of spectral energy, and the width of the peak.

Simulation case	$\langle \delta N_i/N_i \rangle_{rms}$	ΔR_{corr} (cm)	Δz_{corr} (cm)	ω_{max} (rad/s)	$\Delta\omega_{max}$ (rad/s)
#1	0.13/0.07	1.2/1.5	0.6/0.9	3/0.5	4/2
#1a	0.065/0.045	0.7/0.8	2.0/2.3	0/0	1/0.7
#2	0.25/0.12	1.1/1.2	0.5/1.2	0/0	1.5/1
#3	0.17/0.08	1.7/1.9	0.4/1.4	0/0	1.5/1
#4	0.20/0.12	1.4/1.2	0.6/2	0/0	3.5/3
#5	0.21/0.12	1.7/2.0	0.4/0.7	3.0/1.5	2/1.2
#6a	0.07/0.05	1.5/1.7	0.8/0.9	0.5/0.5	0.5/0.5
#6b	0.011/0.006	0.5/0.6	3/3	3.8/3.8	0.25/0.25
BES Data	0.09 ± 0.2	2 ± 0.2	2 ± 0.2	3.8	1.32 ± 0.2

diffusivities in the simulations for case 5 agree within factors of 2 with the diffusivities used in two-dimensional UEDGE simulations to match experimental data for profiles (Table I).

The agreement of the filtered simulation data with BES data shown in Fig. 8 is better than a factor of 2 for the relative density fluctuation amplitude and localization, and for the peak of the density fluctuation power spectrum and its width. The radial half-width of the filtered density correlation function in the simulation is O(1/3) of that measured by BES. The overall comparison of the simulation results with the probe and BES data in Tables I and II shows that the agreement generally improves as more physics is added in the progression from cases 1 to 5. Note that perpendicular correlation lengths of order 1–2 cm, broadband spectra 10–100 kHz, and fluctuation levels 10%–50% seen in the DIII-D data and the simulations here are typical of scrape-off-layer turbulence and have been observed in other tokamaks and in gyrofluid simulations.[39]

No significant power is observed in the saturated density fluctuation power spectrum beyond a radial wavenumber magnitude equal to 5 rad/cm in the simulations (the Nyquist wavenumber is $2.5\times$ larger than this) as shown in Fig. 9. The power spectra are relatively isotropic with respect to the wavenumbers k_r and the binormal k_z. This is reproduced with the number of radial cells increased from 40 to 80; again no significant spectral energy is observed in the power spectrum for radial wavenumbers greater than for $|k_r| \sim 5$ rad/cm. Moreover, the saturated amplitudes for the density, temperature, and potential fluctuations at the separatrix in the simulation with $2\times$ radial resolution are within 10%-20% of those with the coarser radial grid. The cell size with 40 radial cells is ~ 0.25 cm, which is $5\times$ the ion Larmor radius at 100 eV and $B_0 = 2$ T for hydrogen, $\rho_s \sim 0.05$ cm However, the spectra for the turbulence indicates that there is negligible energy at scales shorter than or equal to the grid scale, which suggests that the ion Larmor radius spatial scale is not relevant in the spectrum of the turbulent fluctuations.

Next, the influence of an imposed radial electric field derived from ϕ_0 and the concomitant imposed zonal flow on the edge turbulence is investigated. The model of E_{r0} used here is based on fitting an axisymmetric scalar electric potential to charge-exchange re-emission (CER)[40] and edge Langmuir probe data. Because the domain extends to smaller radii than are accessible to the probe, extrapolation of the structure of the E_{r0} inferred from the probe to smaller radii in such a way as to fit the CER data is challenging. The CER data have temporal scatter and lower spatial resolution than does the Langmuir probe. The model for E_{r0} retains terms in a polynomial expansion of the electric potential through the second radial derivative determined from a smooth fit to the probe data and extrapolates smoothly to smaller radii (Fig. 10). The detailed E_{r0} structure from the probe data near
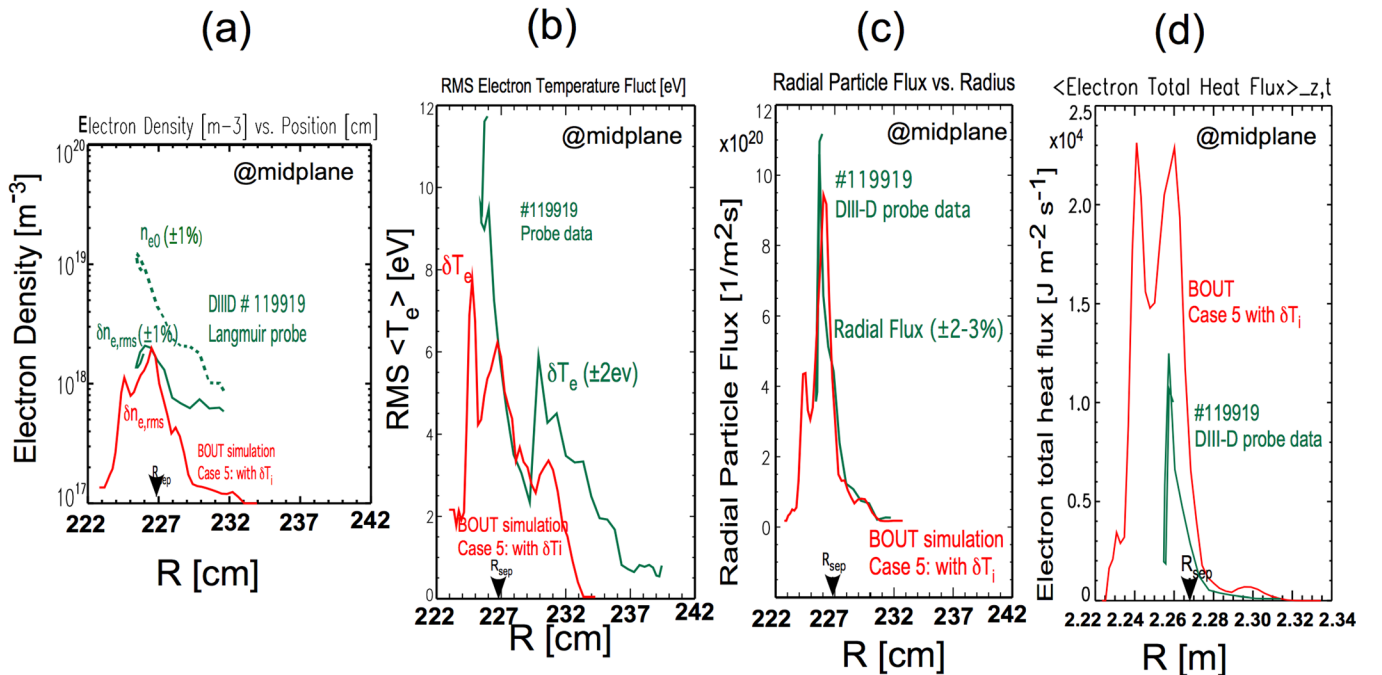

FIG. 7. Comparison to probe data (green) to case 5 simulation (red) of shot #119 919 for (a) electron density and (b) electron temperature fluctuations, (c) radial particle flux, and (d) total electron radial heat flux vs. probe radius position at the midplane.
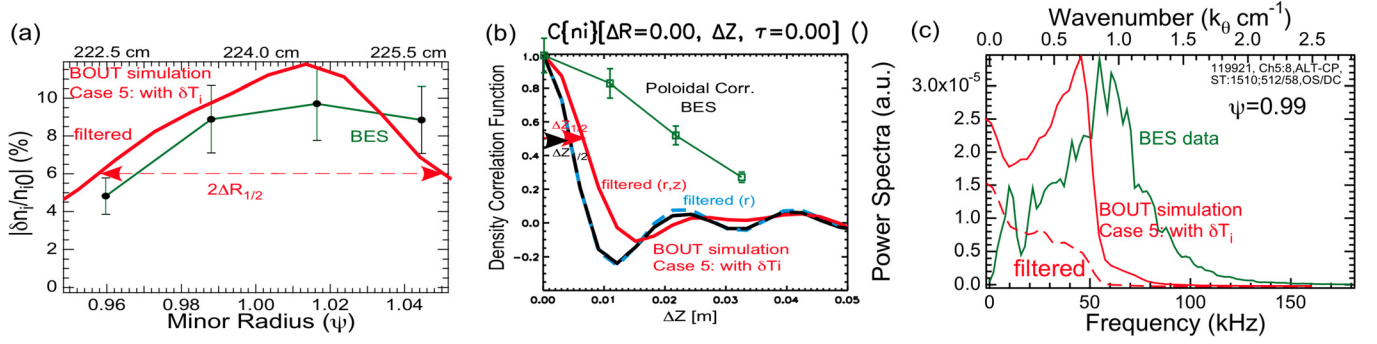
FIG. 8. Shot #119 919. Comparison of BES data (green) to synthetic diagnostics for case 5 simulation (red) for (a) relative electron density vs. radius near midplane, (b) density correlation function vs. Δz separation, and (c) density fluctuation power spectrum vs. frequency.

the separatrix in the model is not retained in this fit. The CER data neither confirm nor refute the structure seen in the probe data near the separatrix. The shearing rate determined by dV_E/dr in the model is shown in Fig. 10(c), where V_E is the radial component of the $\mathbf{E} \times \mathbf{B}$ velocity. Note that the maximum shearing rate in the model is $\sim 2.4 \times 10^4 \text{s}^{-1}$, which is significantly smaller (by a factor of 4) than the observed linear growth rates in the BOUT simulations which are $O(1) \times 10^5 \text{ s}^{-1}$. The temporal evolution of the root-mean-square electron density fluctuation and electric potential amplitudes for case 1 (no temperature fluctuations) is shown in Fig. 11(a) with and without the imposed E_{r0}. Similar plots are shown in Fig. 11(b) with the inclusion of the T_e fluctuation amplitude for cases 4, 5, and 6. With E_{r0} imposed, the linear growth rates are weaker; and saturation is delayed. Figure 11(a) shows that the fluctuation amplitudes are still drifting to higher values when the simulation with finite E_{r0} was terminated. The simulations in Fig. 11(b) show modest reductions in saturated amplitudes for finite E_{r0} and substantial reductions for $5 \times E_{r0}$ for the durations of these simulations. The quantitative agreement of case 6 to probe and BES data is worse than for case 5 ($E_{r0} = 0$) in Tables I and II. With $5 \times E_{r0}$ the maximum shearing rate exceeds the observed growth rate in the absence of the sheared V_E; and the stabilizing effect

of the flow shear is profound (Figs. 11(a) and 11(b)), which is in keeping with the established paradigm.[41]

In Figure 12, a different visualization of the simulation results for cases 5 and 6 for #119 919 is provided. Figure 12 represents the probe and simulation data with respect to the BOUT radial position in the midplane of the BOUT simulation geometry as in Figs. 2–5, 10, and 16, which is offset by $+1.5$ cm from the probe radial position located a few cm below the midplane. The radial position is corrected to the midplane in Figs. 7, 14, and 17. The vertical error bars on the simulation data in Fig. 12 represent the temporal variability of the fluctuation-related quantities in the saturated state. Other simulations have been undertaken with a different model E_{r0}, which show complete recovery of the saturation amplitudes obtained with $E_{r0} = 0$ when the simulations are run long enough. The long-time effects of an imposed E_{r0} for this and other models of E_{r0} merit further study in the future. Moreover, the contributions from self-consistent generation of zonal flows will be included in future work.

Additional simulations have been undertaken examining the influence of alternative boundary conditions on the fluctuating fields ϕ and $A_\parallel$. The additional simulations addressed case 6a (includes both T_e and T_i fluctuations, and E_{r0} with radial boundary conditions $\phi, A_\parallel = 0$ at either the inner or outer radial boundary and $\phi, A_\parallel = 0$ at the other radial boundary, or $d(\phi, A_\parallel)/dx = 0$ at both inner and outer radial boundaries. The simulation results with $\phi, A_\parallel = 0$ at the inner boundary and $d(\phi, A_\parallel)/dx = 0$ at the outer boundary are the same as those obtained in case 6a with $\phi, A_\parallel = 0$ at both radial boundaries. The simulation results with $d(\phi, A_\parallel)/dx = 0$ at both inner and outer radial boundaries are the same as with $d(\phi, A_\parallel)/dx = 0$ at the inner boundary and $\phi, A_\parallel = 0$ at the outer radial boundary, and yield the same linear and nonlinear results as in case 6a with $\phi, A_\parallel = 0$ at both radial boundaries with the exception that a $\pm 10\%$ oscillation with frequency ~ 100 kHz emerges superposed on the fluctuating potential ϕ at saturation but not at a noticeable level in the temperature and density fluctuations. The temporal oscillation is accompanied by a small additional perturbation in the radial profiles of the fluctuations near the inner radial boundary.

C. Edge plasma turbulence in shot #119 934

The second studied shot is DIII-D L-mode discharge #119 934, with the edge plasma somewhat colder and lower
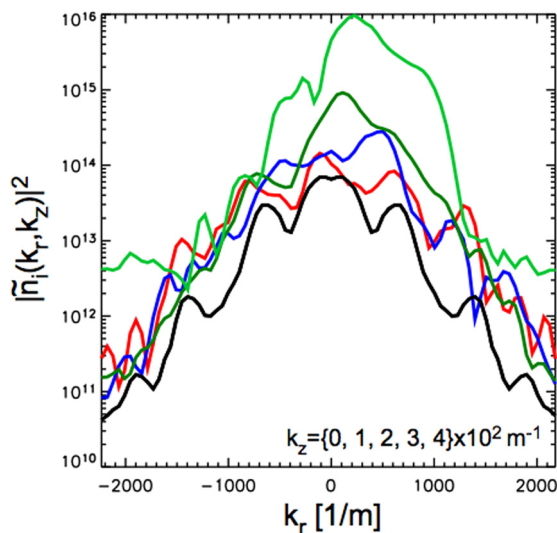

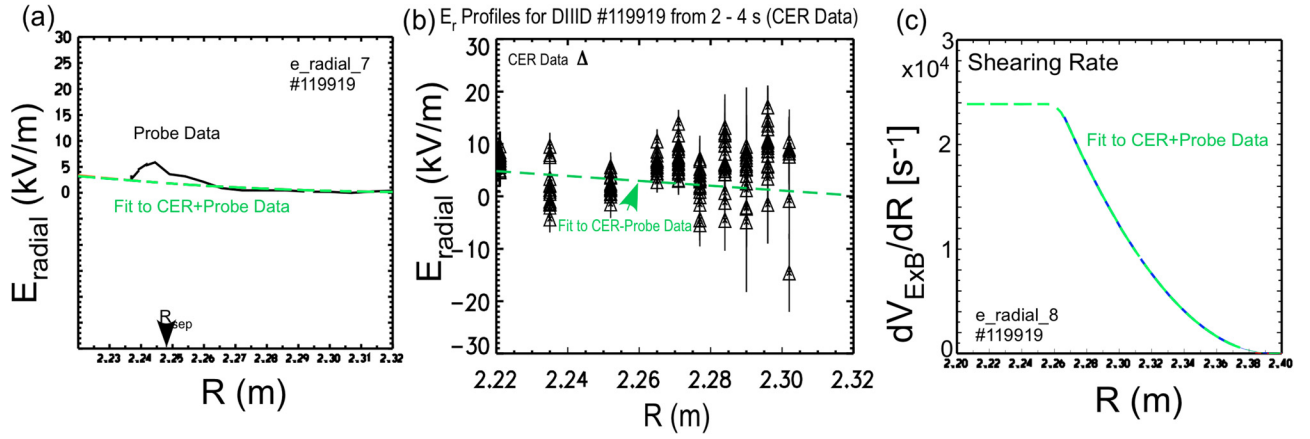FIG. 9. Density fluctuation power spectrum with respect to $[k_r, k_z]$ at saturation for case 5.

FIG. 10. Shot #119 919. Model fit of radial electric field E_{r0} vs. radius in midplane to (a) probe and (b) CER data, and (c) the shearing rate dV_E/dr vs. radius implied by the fitted E_{r0}.

density than in #119 919. Plots of the radial electron density and electron temperature profiles for #119 919, and 119 934 are exhibited in Fig. 13. Discharge #119 934 is more collisional than #119 919 because of the stronger dependence of the collision frequency on the temperature. The growth rate for resistive ballooning from Eq. (31) of Ref. 6 scales as $\eta^{1/3}\beta^{2/3}/n^{1/3} \propto T^{1/6}n^{1/3}$, where η is the classical electrical resistivity, β is the ratio of kinetic energy density to magnetic

energy density, T is the temperature (assume $T_e \approx T_i$ and n is the plasma density). Hence, for $\sim 50\%$ reduced temperature and plasma density, the resistive ballooning growth rate is expected to decrease by $1/\sqrt{2}$; and this is consistent with the simulation results here. In Fig. 14 are plotted the experimental electron density and electron temperature fluctuation amplitudes, the radial electron particle flux, and the total electron thermal flux as functions of major radius from the
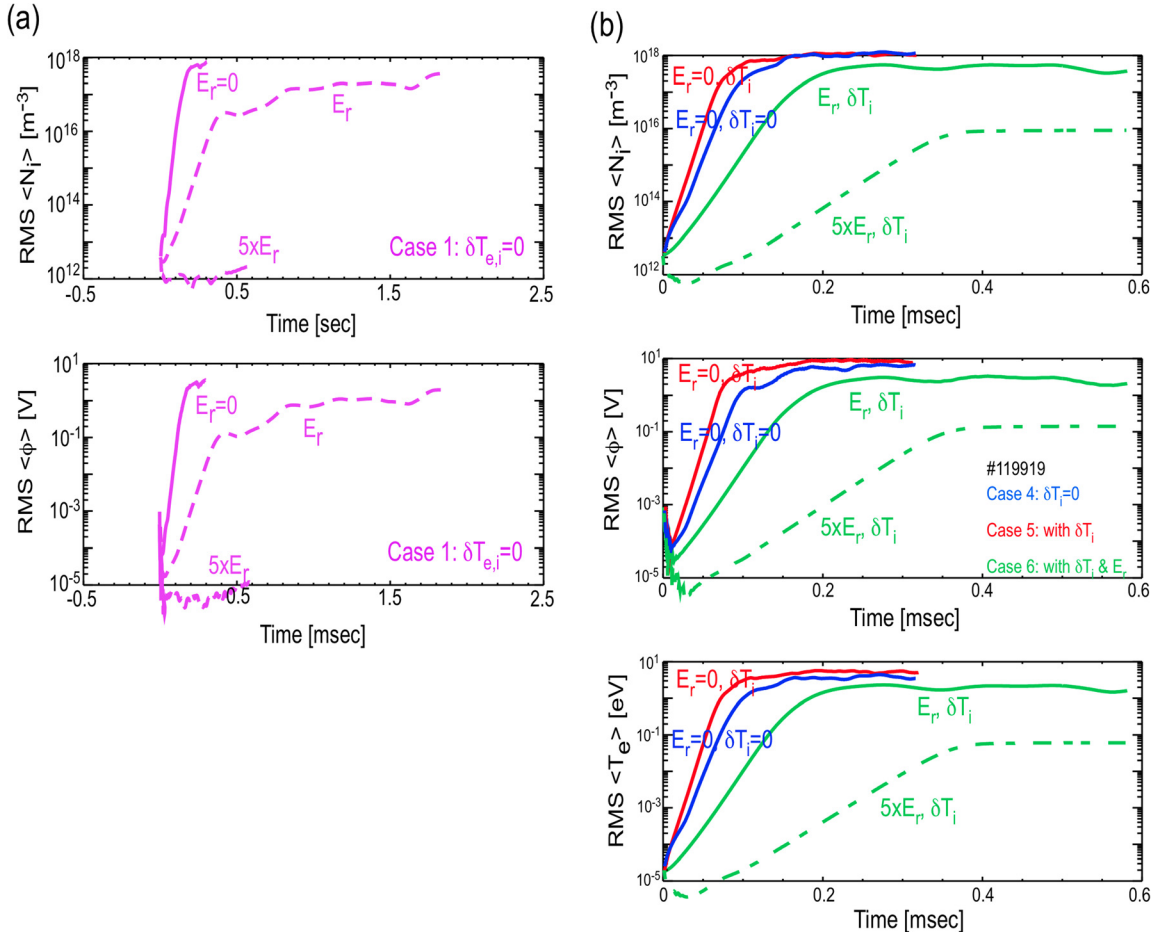

FIG. 11. Shot #119 919. (a) Case 1 with/without E_{r0} simulation histories for RMS ion density and electric potential fluctuations at the separatrix and in the midplane vs. time. (b) Cases 4, 5, and 6 simulation histories for the RMS ion density, electric potential, and electron temperature fluctuations at the separatrix and in the midplane vs time.
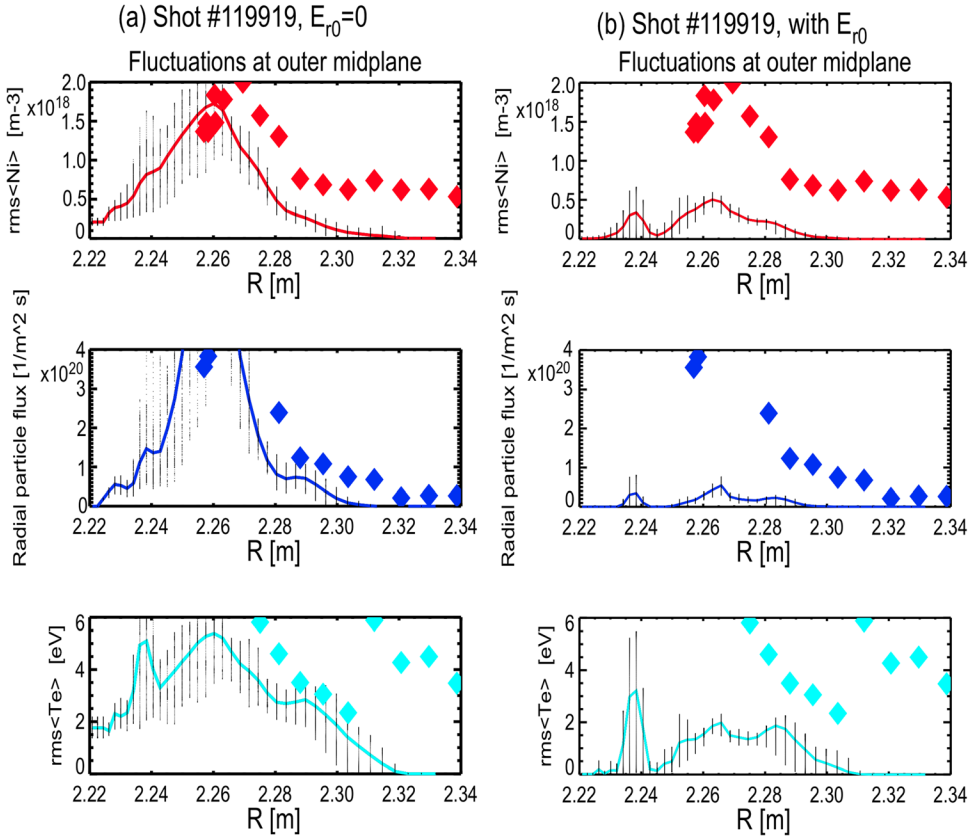
(a) Shot #119919, $E_{r0}=0$
Fluctuations at outer midplane

(b) Shot #119919, with E_{r0}
Fluctuations at outer midplane

FIG. 12. Shot #119 919. (a) Case 5 ($E_{r0} = 0$) simulation RMS ion density, radial particle flux, and electron temperature fluctuations vs. radius in the midplane compared to probe data (diamonds). (b) Case 6 (with E_{r0}) simulation RMS ion density, radial particle flux, and electron temperature fluctuations vs. radius in midplane compared to probe data (diamonds).

probe data near the midplane. In Fig. 14, the fluctuation amplitudes and fluxes are similar in shots #119 930 and 119 934, and smaller than in shot #119 919 consistent with expectation based on consideration of the resistive ballooning growth rate. This is reinforced by the results of the simulations of case 5 with T_e and T_i fluctuations for shots #119 919 and #119 934 whose temporal evolution (Fig. 15) shows modestly reduced growth rates (reductions of ~20%) and somewhat lower RMS fluctuation amplitudes in the midplane for shot #119 934. In comparing Figs. 7 and 16, it can be

seen that the turbulent fluctuations have similar radial extents in both the #119 919 simulation and #119 934 experimental data. Radial plots of the fluctuation amplitudes and fluxes in the outer midplane at saturation from the case 5 simulation with T_e and T_i fluctuations are also compared to probe data from #119 934 in Fig. 16.

In Fig. 17 are plotted the turbulent particle flux and the conductive and convective components of the energy fluxes as functions of the probe radial position for the case 5 simulations (with $T_{e,i}$ fluctuations and $E_r = 0$) of discharges #119 919 and #119 934. The fluxes are lower in the lower-temperature, lower-density #119 934 plasma. The simulations and the probe data generally agree within a factor of 2 for the density and temperature fluctuations, the radial particle flux, and the electron total heat flux. Because the total particle flux in the simulation agrees within a factor of 2 with the probe data, so does the convective heat flux; and the agreement of the total heat flux summed over the convective and conductive components between experiment and simulation is significantly better than for the conductive heat flux alone. The turbulence in the midplane peaks just inside the separatrix, apparently driven by the strong gradients there and the longer connection length.

In Fig. 18 is shown a simple fit of the radial electric field E_{r0} to the probe and CER data for shot #119 934. As with the fit of E_{r0} to the data for shot #119 919, the sharp structure seen in E_{r0} in the probe data inside the separatrix is again omitted; and a smooth second radial derivative of the electric potential to smaller radii is extrapolated so that there is a good fit to the CER data at radii inside the separatrix (Fig. 18). Deferred to future work is the incorporation into the
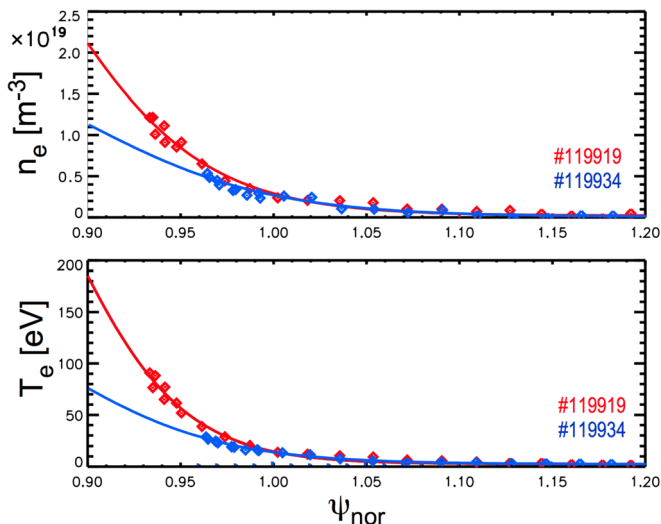
FIG. 13. Fits to (a) ion density and (b) electron temperature radial profiles in midplane for shots #119 919 (red) and 119 934 (blue) used in simulations. Langmuir probe data are shown by diamonds.
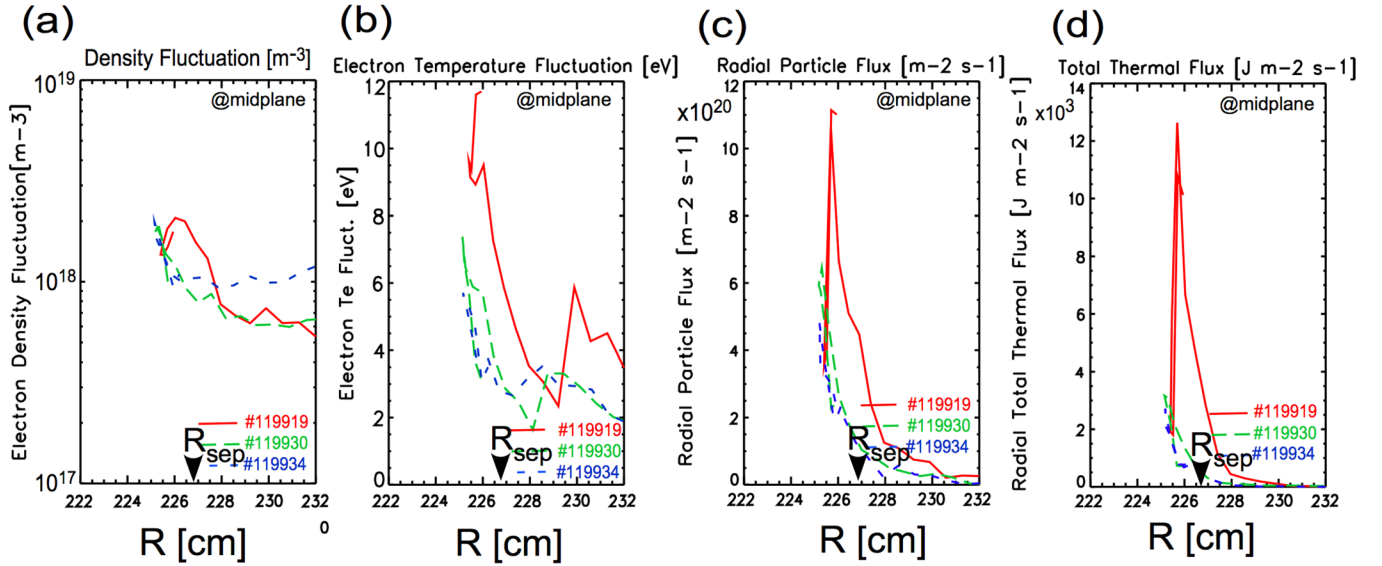
FIG. 14. Comparison of probe data for (a) electron density and (b) electron temperature fluctuations, (c) radial particle flux, and (d) total electron radial heat flux vs. probe position at the midplane data for shots #119 919 (red), 119 930 (green), and 119 934 (blue).

model of the detailed structure of E_{r0} near the separatrix seen by the probe. Comparisons of the results of BOUT simulation case 6a with the inclusion of E_{r0} to the results of case 5 for shot #119 934 are shown in the time history of the RMS fluctuation amplitudes in Fig. 19. The linear growth rate is reduced with the inclusion of E_{r0} in the simulation, but the turbulence eventually recovers fluctuation amplitudes that are comparable to case 5 with $E_{r0} = 0$ (Fig. 19). The density

and electron temperature fluctuation amplitudes are modestly higher in the probe data than in the simulations, and the influence of finite E_{r0} is weak (Fig. 16). The electron particle and total thermal fluxes based on the probe data cut through the simulation data (Fig. 16), and these fluxes at the end of the simulation shown in Fig. 18 are lower compared to the case with $E_{r0} = 0$ by factors of 2-4 in the case with finite E_{r0}. Overall the agreement of the simulations with finite E_{r0} and $E_{r0} = 0$ with the probe data is within factors of 2-3 or better for shot #119934.

An additional simulation of case 6 (with electron and ion temperature fluctuations and E_{r0}) for #119 934 conditions was undertaken with a modification of the model equations, Eqs. (1) and (2), in which $A_\parallel = 0$, i.e., a purely electrostatic model for resistive drift ballooning. Given that the edge plasma is low β, $\beta < 10^{-4}$ for $T_e \sim 50\,\mathrm{eV}$, $n \sim 10^{13}\,\mathrm{cm}^{-3}$, and $B_0 \sim 2\,\mathrm{T}$, where β is the ratio of thermal energy density to magnetic energy density) such that $\beta m_i/m_e \ll 1$, it is expected that the electromagnetic modifications should be weak. Indeed, the purely electrostatic simulation yields results for the turbulent fluctuations that differ less than 10%-20% from the results of the electromagnetic model case 6 shown in Figures 15 and 16, which is well within the temporal variability of the observables at saturation.

IV. DISCUSSION AND CONCLUSIONS

In this work simulation results and comparison to L-mode discharge data from DIII-D in the edge region straddling the last closed flux surface are reported. This work can be viewed as a validation exercise for a turbulence simulation using Braginskii-based simplified plasma-fluid equations applied to the study of the edge turbulence in DIII-D L-mode discharges. These model equations are based on the drift-resistive ballooning physics model evolved from the earlier work of Carreras *et al.*, and Guzdar *et al.*, and implemented in BOUT in a realistic, single-null geometry for DIII-D with conditions specific to a few well-characterized
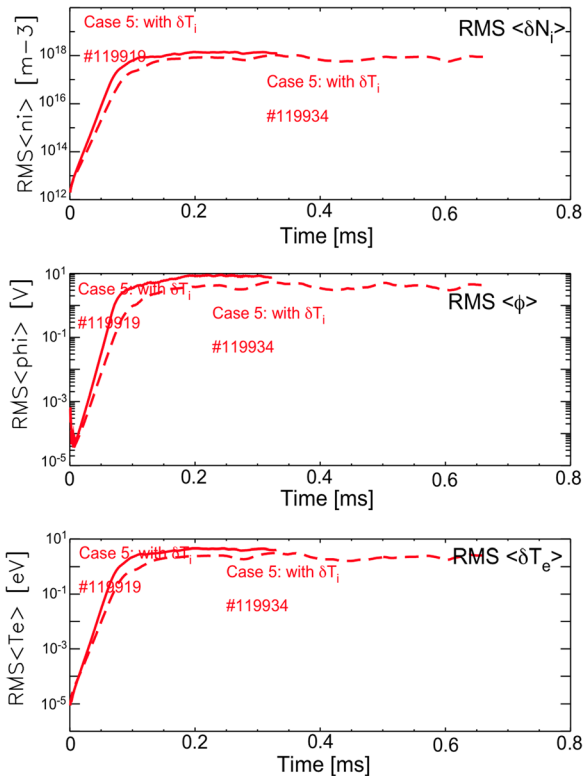

FIG. 15. Histories of the RMS ion density, electric potential, and electron temperature fluctuations at the separatrix and in the midplane in case 4 simulations of shots #119 919 (solid line) and colder, lower density plasma 119 934 (dashed line).
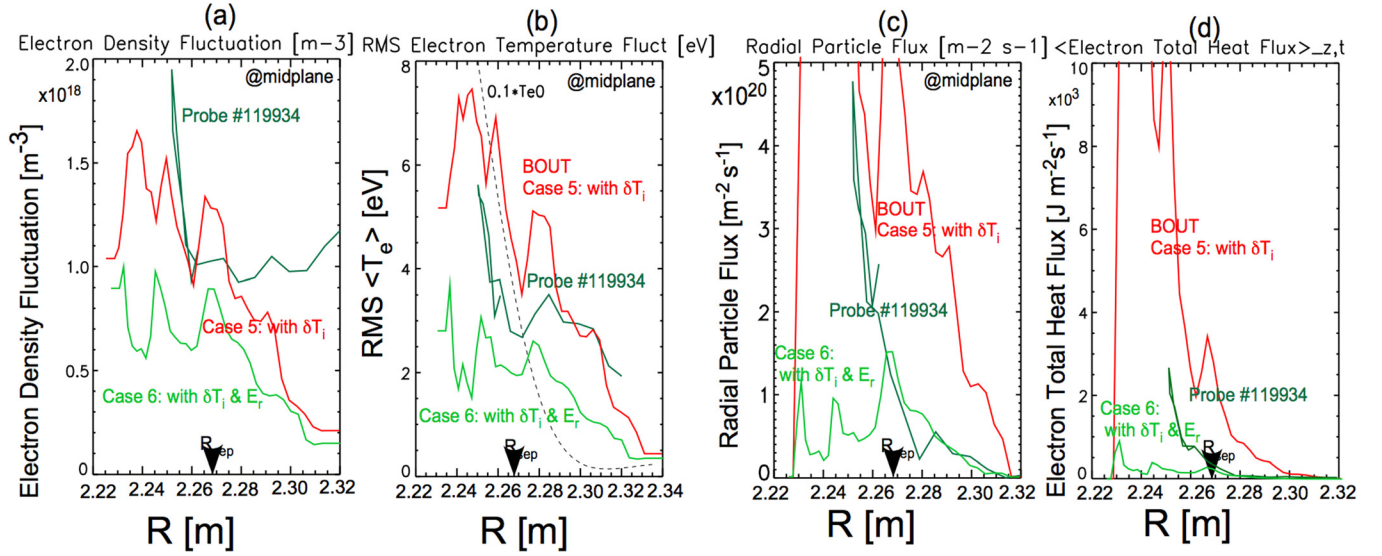
FIG. 16. Comparison of probe data (dark green) and case 5 (red) and case 6 (green) simulation data for (a) electron density and (b) electron temperature fluctuations, (c) radial particle flux, and (d) total electron radial heat flux vs. probe position at the midplane data for shot #119 934.

L-mode discharges. Presented are detailed comparisons of the simulation results to data provided by a scanning Langmuir probe and by beam-emission spectroscopy (BES) where available for DIII-D L-mode shots #119 919 and 119 934. Shot #119 930 has lower edge plasma density and electron temperature than in #119 919, and is found to be less unstable and less turbulent in both the experiment and the simulations. The simulations of shot #119 934 yield growth rates ~20% less than those observed for the conditions of

#119 919, generally consistent with the 30% reduction in the resistive ballooning growth rate because of the lower temperature and density in discharge #119 934. There are also results from a simulation of #119 934 with an imposed E_{r0} in which the physics model is purely electrostatic, and these results are substantially the same as those in the corresponding electromagnetic simulation. These results suggest that electromagnetic effects are generally unimportant for the low-β L-mode plasma conditions simulated.
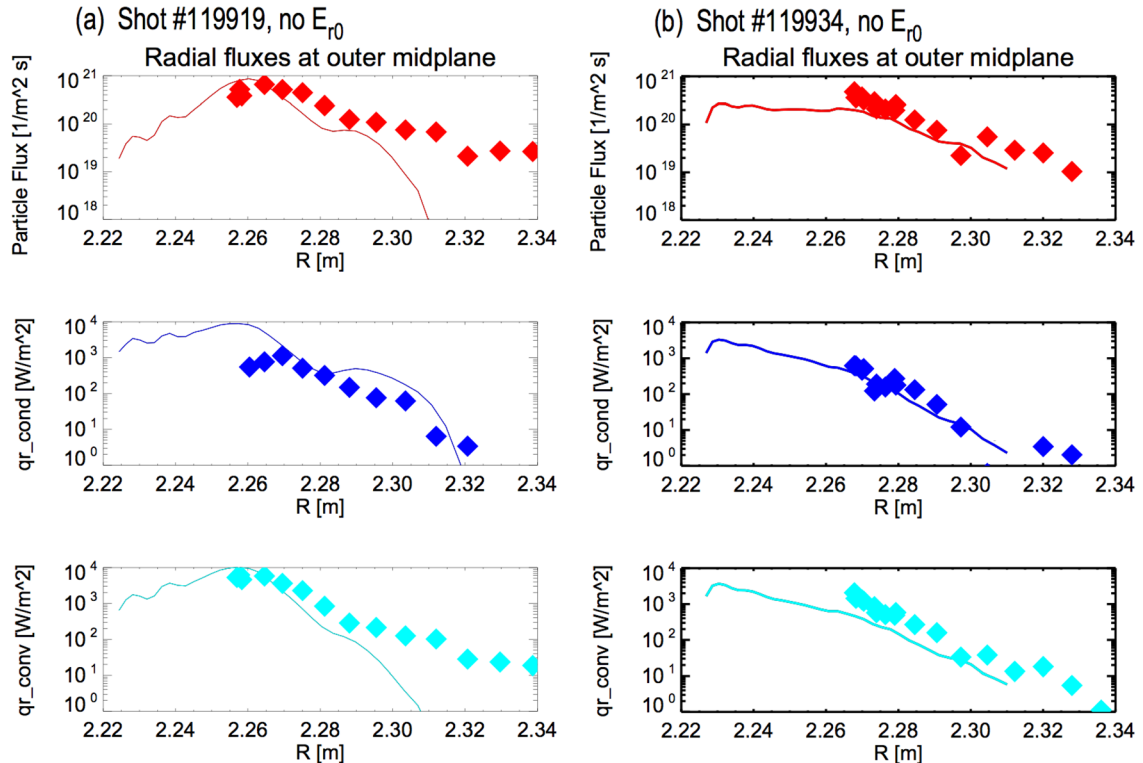

FIG. 17. RMS radial particle flux, conductive and convective radial thermal fluxes vs. radius in the midplane compared to probe data (diamonds) for case 5 ($E_{r0} = 0$) simulations of shots (a) #119 919 and (b) colder, lower density plasma #119 934. The approximate location of the separatrix in the outer midplane is at 2.265 m.
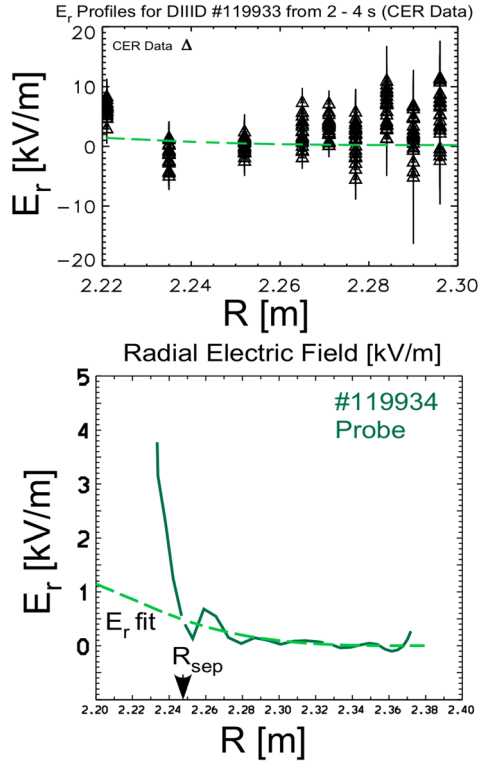
FIG. 18. Model fit of radial electric field E_{r0} vs. radius in midplane to probe and CER data for shot #119 934.

The principal findings here are that simulations based on the drift-resistive ballooning model yield results for fluctuation amplitudes, particle and heat fluxes, inferred radial diffusivities, correlation lengths, and spectra that agree within an order of magnitude with the DIII-D L-mode experimental data and within a factor of 2 in some cases (see Figures 7, 8, 11, 15, and 16; and Tables I and II). Moreover, the agreement tends to improve in the progression from cases 1 to 5 (Tables I and II). A lower density and lower temperature plasma is less unstable and less turbulent. Imposing a radial electric field in the simulations, based on a simple model fit to the probe and BES data from DIII-D, adds a sheared $\mathbf{E} \times \mathbf{B}$ zonal flow that reduces the linear growth rates observed in the simulations. In the simulations of #119 919 the saturated turbulence with finite E_{r0} is at moderately smaller amplitudes, while in the simulations of #119 934

with E_r the turbulence recovers and saturates at amplitudes very close to those observed with $E_{r0} = 0$. That the stabilizing effects of E_r on the turbulence and the saturation amplitudes are either modest or very weak is in keeping with the fact that the shearing rates due to E_{r0} are much smaller than the linear growth rates. However, for the imposed electric field E_{r0} scaled up by a factor of 5 there is a drastic (several orders of magnitude) reduction in the saturated turbulence levels over the time simulated. This value of E_{r0} corresponds to a shearing rate that is comparable to the linear growth rates and the turbulence characteristic frequencies, and this is where one would indeed expect the E_{r0} shearing to have a strong effect.

Remarkably, the turbulence fully recovers in the case 6a simulation of #119 934 with finite E_{r0} and not in the case 6a simulation of #119 919 with finite E_{r0} over the length of time simulated. Although #119 934 case 6a simulation has a weaker linear growth rate than in the #119 934 case 5 simulation, in the nonlinear saturation these simulations are similar, which is perhaps qualitatively consistent with observations in a number of earlier published studies showing that nonlinear instabilities in drift-wave turbulence simulations can supersede linear instabilities in determining saturated turbulence.[42–46]

In these turbulence simulations, an imposed time-independent E_{r0} produces a sheared zonal flow. This is very different from drift turbulence in a periodic cylinder system, e.g., in the Hasegawa-Wakatani studies,[47,48] or in tokamak core gyrokinetic simulation studies,[49] where the E_{r0} is generated by turbulence itself via the Reynolds stress. In these two examples, the self-consistent zonal flow is of key importance for turbulence saturation. In contrast, we note that inclusion of the turbulence generated zonal flow may have little effect on saturated turbulence and transport in some instances, e.g., in the study of Holland *et al.* of electron temperature gradient instability there is no significant zonal flow formation exhibited.[50] Moreover, in the tokamak edge there may be a number of mechanisms, other than the turbulence generated Reynolds stress, which can contribute to or, in some regimes, perhaps completely dominate the E_r. In particular, in the tokamak scrape-off layer the radial electric field is strongly influenced by the sheath boundary conditions on the target plates, finite ion-orbit loss, charge exchange with neutrals,
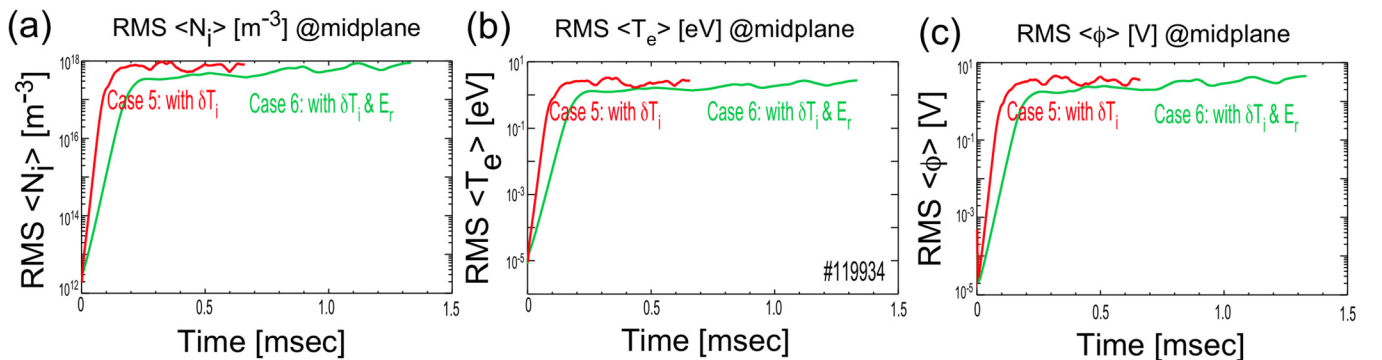

FIG. 19. Cases 5 ($E_{r0} = 0$) and 6 (with E_{r0}) simulation data for histories of the RMS (a) ion density, (b) electron temperature, and (c) electric potential fluctuations at the separatrix in the midplane for shot #119 934.

TABLE III. Fit coefficients for the profiles $N_{i0}(\hat{\psi})$, T_{e0}, ϕ_0 used in the simulations.

Shot	Profile	a_0	a_1	a_2	a_3	a_4
#119 919	N_{i0}	2.89×10^{19}	2.87×10^{19}	8.77×10^{-1}	8.07×10^{-2}	-3.78×10^{-2}
#119 919	T_{e0}	2.33×10^{2}	2.31×10^{2}	8.87×10^{-1}	6.25×10^{-2}	-1.10×10^{-2}
#119 919	ϕ_0	3.31×10^{2}	3.26×10^{2}	8.85×10^{-1}	7.20×10^{-2}	-3.33×10^{-1}
#119 934	N_{i0}	1.16×10^{19}	1.16×10^{19}	8.96×10^{-1}	9.94×10^{-2}	-1.93×10^{-2}
#119 934	T_{e0}	9.52×10^{1}	9.40×10^{1}	8.80×10^{-1}	9.43×10^{-2}	-1.81×10^{-1}
#119 934	ϕ_0	1.06×10^{2}	1.03×10^{2}	9.17×10^{-1}	6.51×10^{-2}	3.29×10^{-2}

and other non-ambipolar effects; how these effects compete with the turbulence generated Reynold's stress contributions to the zonal flows in the edge remains to be determined. It may be possible to extend the edge turbulence model used here by combining an imposed steady-state E_{r0} with time-dependent short wavelength components of turbulence-generated E_{r0}.[51,52] This is the subject of ongoing research that will be reported in a future publication.

APPENDIX: SIMULATION PROFILES

The smoothed fits to the experimental profiles for the plasma density and the electron temperature are shown in Fig. 13 for the experimental discharges. The profiles for the radial electric fields and the fits used in the simulations are shown in Figs. 10 and 18. The fits to the unperturbed density, temperature, and electric potential profiles used in the simulations are given by the following analytic model:

$$f(x) = a_0 + a_1 \frac{(1 + a_4 w)\exp(w) - \exp(-w)}{\exp(w) + \exp(-w)},$$
$$w \equiv (a_2 - x)/a_3, \tag{A1}$$

where $x \equiv \psi_{norm} = (\psi - \psi_{mag\,axis})/(\psi_{sep} - \psi_{mag\,axis})$, ψ_{norm} is the normalized poloidal flux, and the parameters $(a_0, a_1, a_2, a_3, a_4)$ are defined in Table III for the density, electron temperature, and electric potential profiles in simulation of shots #119 919 and 119 934. The expressions for the model density and temperature profiles give high-quality, smooth fits to the experimental profiles shown in Fig.13.

Figures 10 and 18 show the imposed radial electric fields used in the simulations with finite E_{r0}. The two-dimensional magnetic geometry is determined from magnetic reconstructions of the discharges using the DIII-D database. The extent of the radial slice is defined by $0.9 \le \psi_{norm} \le 1.15$.

[1]J. Kinsey, G. Bateman, T. Onjun, A. Kritz, A. Pankin, G. Staebler, and R. Waltz, Nucl. Fusion **43**, 1845 (2003).
[2]M. Kotschenreuther, P. M. Valanju, S. M. Mahajan, and J. C. Wiley, Phys. Plasmas **14**, 72502 (2007).
[3]J. Luxon, Nucl. Fusion **42**, 614 (2002).
[4]A. Wooton, B. Carreras, H. Matsumoto, K. McGuire, W. Peebles, C. Ritz, P. Terry, and S. Zweben, Phys. Fluids B **2**, 2879 (1990).
[5]B. Carreras, P. Diamond, M. Murakami, J. Dunlap, J. Bell, H. Hicks, J. Holmes, E. Lazarus, V. Pare, P. Similon *et al.*, Phys. Rev. Lett. **50**, 503 (1983).
[6]B. Carreras, L. Garcia, and P. Diamond, Phys. Fluids **30**, 1388 (1987).
[7]P. Guzdar, J. Drake, D. McCarthy, A. Hassam, and C. Liu, Phys. Fluids B **5**, 3712 (1993).
[8]S. Novakovskii, P. Guzdar, J. Drake, and C. Liu, Phys. Plasmas **2**, 3764 (1995).
[9]P. Guzdar and A. Hassam, Phys. Plasmas **3**, 3701 (1996).
[10]B. Rogers, J. Drake, and A. Zeiler, Phys. Rev. Lett. **81**, 4396 (1998).
[11]P. Guzdar, R. Kleva, R. Groebner, and P. Gohil, Phys. Plasmas **11**, 1109 (2004).
[12]H. Furth, J. Killeen, and M. Rosenbluth, Phys. Fluids **6**, 459 (1963).
[13]B. Coppi, Phys. Fluids **7**, 1501 (1964).
[14]X. Xu and R. Cohen, Contrib. Plasma Phys. **38**, 158 (1998).
[15]X. Xu, R. Cohen, T. Rognlien, and J. Myra, Phys. Plasmas **7**, 1951 (2000).
[16]M. V. Umansky, R. H. Cohen, L. L. LoDestro, and X. Q. Xu, Contrib. Plasma Phys. **48**, 27 (2008).
[17]B. D. Dudson, M. V. Umansky, X. Q. Xu, P. B. Snyder, and H. R. Wilson, Comput. Phys. Commun. **180**, 1467 (2009).
[18]J. Boedo, D. Rudakov, R. Moyer, S. Krasheninnikov, D. Whyte, G. McKee, G. Tynan, M. Schaffer, P. Stangeby, P. West *et al.*, Phys. Plasmas **8**, 4826 (2001).
[19]J. A. Boedo, N. Crocker, L. Chousal, R. Hernandez, J. Chalfant, H. Kugel, P. Roney, J. Wertenbaker, and N. Team, Rev. Sci. Instrum. **80**, 123506 (2009).
[20]J. A. Boedo, J. Nucl. Mater. **390–391**, 29 (2009).
[21]D. Gupta, R. Fonck, G. McKee, D. Schlossberg, and M. Shafer, Rev. Sci. Instrum. **75**, 3493 (2004).
[22]G. R. McKee, R. J. Fonck, M. W. Shafer, I. U. Uzun-Kaymak, and Z. Yan, Rev. Sci. Instrum. **81**, 10D741 (2010).
[23]G. R. McKee, P. Gohil, D. J. Schlossberg, J. A. Boedo, K. H. Burrell, J. S. deGrassie, R. J. Groebner, R. A. Moyer, C. C. Petty, T. L. Rhodes *et al.*, Nucl. Fusion **49**, 115016 (2009).
[24]S. Braginskii, "Transport processes in a plasma," Rev. Plasma Phys. **1**, 205 (1965).
[25]B. D. Scott, Plasma Phys. Controlled Fusion **49**, S25 (2007).
[26]T. Rafiq, C. C. Hegna, J. D. Callen, and A. H. Kritz, Phys. Plasmas **16**, 102505 (2009).
[27]X. Q. Xu, M. V. Umansky, B. Dudson, and R. B. Snyder, Comm. Comp. Phys. **4**, 949 (2008).
[28]M. V. Umansky, X. Q. Xu, B. Dudson, L. L. LoDestro, and J. R. Myra, Comput. Phys. Commun. **180**, 887 (2009).
[29]T. Rognlien, J. Milovich, M. Rensink, and G. Porter, J. Nucl. Mater. **196**, 347 (1992).

[30]D. A. Baver, J. R. Myra, and M. V. Umansky, Comput. Phys. Commun. **182**, 1610 (2011).

[31]P. Popovich, M. V. Umansky, T. A. Carter, and B. Friedman, Phys. Plasmas **17**, 102107 (2010).

[32]P. Diamond, S.-I. Itoh, and K. Itoh, *Modern Plasma Physics*, Vol. 1 (Cambridge University Press, Cambridge, United Kingdom, 2010).

[33]J. Terry, S. Zweben, K. Hallatschek, B. LaBombard, R. Maqueda, B. Bai, C. Boswell, M. Greenwald, D. Kopon, W. Nevins *et al.*, Phys. Plasmas **10**, 1739 (2003).

[34]C. Ritz, R. Bravenec, P. Schoch, R. Bengston, J. Boedo, J. Forster, K. Gentle, Y. He, R. Hickok, Y. Kim *et al.*, Phys. Rev. Lett. **62**, 1844 (1989).

[35]D. Rudakov, J. Boedo, R. Moyer, R. Lehmer, G. Gunner, and J. Watkins, Rev. Sci. Instrum. **72**, 453 (2001).

[36]D. A. D'Ippolito, J. R. Myra, and S. J. Zweben, Phys. Plasmas **18**, 60501 (2011).

[37]W. M. Nevins, *GKV User's Manual*, Lawrence Livermore National Laboratory Technical Report, UCRL-TR-206016 (August 2004).

[38]W. M. Nevins, J. Candy, S. Cowley, T. Dannert, A. Dimits, W. Dorland, C. Estrada-Mila, G. W. Hammett, F. Jenko, M. J. Pueschel *et al.*, Phys. Plasmas **13**, 122306 (2006).

[39]S. J. Zweben, B. D. Scott, J. L. Terry, B. LaBombard, J. W. Hughes, and D. P. Stotler, Phys. Plasmas **16**, 82505 (2009).

[40]P. Gohil, K. Burrell, and T. Carlstrom, Nucl. Fusion **38**, 93 (1998).

[41]T. Hahm and K. Burrell, Phys. Plasmas **2**, 1648 (1995).

[42]A. Zeiler, D. Biskamp, J. Drake, and P. Guzdar, Phys. Plasmas **3**, 2951 (1996).

[43]A. Zeiler, J. Drake, and D. Biskamp, Phys. Plasmas **4**, 991 (1997).

[44]B. Scott, Plas. Phys. Controlled. Fusion **45**, A385 (2003).

[45]B. Scott, Phys. Plasmas **12**, 62314 (2005).

[46]B. Friedman, T. A. Carter, M. V. Umansky, D. Schaffner, and B. Dudson, Phys. Plasmas **19**, 102307 (2012).

[47]A. Hasegawa and M. Wakatani, Phys. Rev. Lett. **50**, 682 (1983).

[48]A. Hasegawa and M. Wakatani, Phys. Rev. Lett. **59**, 1581 (1987).

[49]A. Dimits, G. Bateman, M. Beer, B. Cohen, W. Dorland, G. Hammett, C. Kim, J. Kinsey, M. Kotschenreuther, A. Kritz *et al.*, Phys. Plasmas **7**, 969 (2000).

[50]C. Holland, P. Diamond, S. Champeaux, E. Kim, O. Gurcan, M. Rosenbluth, G. Tynan, N. Crocker, W. Nevins, and J. Candy, Nucl. Fusion **43**, 761 (2003).

[51]R. Waltz, J. Candy, and M. Rosenbluth, Phys. Plasmas **9**, 1938 (2002).

[52]R. Waltz, J. Candy, F. Hinton, C. Estrada-Mila, and J. Kinsey, Nucl. Fusion **45**, 741 (2005).

[53]L. L. Lao, H. St. John, R. D. Stambaugh, A. G. Kellman, and W. Pfeiffer, Nucl. Fusion **25**, 1611 (1985).